DESIGN, FABRICATION, AND CHARACTERIZATION OF POLYMER-BASED CANTILEVER PROBES FOR ATOMIC FORCE MICROSCOPY OF LIVE MAMMALIAN CELLS IN LIQUID

By

FANGZHOU YU

A thesis submitted to the

Graduate school-New Brunswick

Rutgers, the State University of New Jersey

In partial fulfillment of the requirements

For the degree of

Master of Science

Graduate Program in Electrical and Computer Engineering

Written under the direction of

Jaeseok Jeon

And approved by

_____

_____

_____

_____

New Brunswick, New Jersey

October 2016

ABSTRACT OF THE THESIS

Design, Fabrication, and Characterization of Polymer-Based Cantilever Probes for Atomic Force Microscopy of Live Mammalian Cells in Liquid

by

FANGZHOU YU

Thesis Director:

Jaeseok Jeon

This thesis presents the design, fabrication, and characterization of polymer-based cantilever probes for atomic force microscopes (AFMs), in order to enable biological research requiring non-destructive high-speed high-resolution topographical imaging and nanomechanical characterizations of sub-cellular and cellular samples. A reliable low-cost surface-micromachining process is developed for the rapid prototyping of bio-compatible polymer-based V-shaped AFM probes. The physical properties of fabricated prototypes, such as effective spring constant, resonant frequency, and quality factor, are determined experimentally via thermal noise method and analytically via finite element and parallel-beam approximation methods. Using a prototype, AFM nanoindentation measurements are performed on live mammalian cells—human cervical epithelial cancer cells (called "HeLa") in a liquid culture medium. Experimental results are compared to those obtained using a commercial Si-based probe; when the prototype probe is used, the deformation and/or distortion of the cell membrane are reduced significantly albeit repeated indentations on the cell surface. For further AFM-based biological studies, the

design and fabrication process of the prototype probe are fine-tuned; a reasonably straight cantilever with a strain gradient as low as 10^{-4} μm^{-1} is achieved via corrugating the optical reflection coating or confining it to the tip region, and a sharp tip with a radius of curvature as small as ~40 nm, which is comparable to that of a Si-based probe, is achieved via sequential depositions of low- and high-viscosity acrylic polymers.

Acknowledgments

First, I would like to express the deepest appreciation to my advisor Prof. Jaeseok Jeon for his support, patience, and guidance in my research towards completing my master's thesis. Without his guidance and persistent help, this dissertation would not be possible. I would like to thank my committee members, Prof. Zoran Gajic, Prof. Qingze Zou, and Prof. Mehdi Javanmard for their evaluation on my research work. Without their direction, I would not have been able to complete my master's thesis.

It is my pleasure to work with selfless and professional people in this project. I would like to thank Yanbiao Pan and Jiangbo Liu for helping me with design and testing. Their countless inputs make this project come true. I would like to thank Zhengyu Yang and Nabeela Khan for simulation section. I would also like to thank Ai-Lian Lin and Shiyan Yu for their assistance in device fabrication and testing.

I am also indebted to all the staff and co-workers in Microelectronics Research Laboratory (MERL) of Rutgers University and Center for Functional Nanomaterials (CFN) of Brookhaven National Lab. Specially thanks to Robert Lorber, Pavel Reyes, Ming Lu, Wen-Chiang Hong, and Rui Li for their training and valuable advice on my project.

Finally, I would like to thank my parents and my fiancée for their support and encouragement to pursue my research.

Table of Contents

List of Tables

List of Figures

Chapter 1

INTRODUCTION

1.1 Silicon-based AFM cantilever probe

Si-based and Si_3N_4-based cantilever probes have been predominantly used today for atomic force microscope (AFM) system of sub-cellular and cellular samples [1]-[3]. The silicon-based cantilever probe, however, tends to be too stiff for live cells, since the elastic modulus of Si is over five orders of magnitude larger than that of live cells [4], [5], thereby imposing severe limitations on imaging the topography and measuring the mechanical properties of live cells. Minimizing deformation/distortion to the cell membrane requires a very low scan rate (~ 0.1 Hz) that translates to an imaging time of 1.5 hours for 512 lines per image frame. Nanomechanical measurements of live mammalian cells are also limited. Elastic modulus measurements are performed at a low force load rate (< 10 Hz). Indentation depth is limited to only a few nanometers in force-distance measurement. And frequency bandwidth of the probe (less than a couple hundred Hz) is narrow for AFM operations on live cells in liquid [6]-[12]. Such scan-rate-limited imaging and frequency-limited mechanical measurements would be inadequate for capturing and characterizing dynamic evolutions of live mammalian cells [9] (e.g., endocytosis process[10]), which typically occur in seconds or minutes, and unsuitable for measuring the frequency-dependent viscoelasticity of live cells [11] since this requires repetitive indentations at the same location of the cell membrane. With current Si-based probes, such a repetitive same-location indentation can lead to damage and break-down of the cell membrane. Given the same design and dimensions, the polymer-based cantilever probe would be much softer than a Si-based one as the elastic modulus of polymers is orders of magnitude lower than that of Si. Thus, it would be advantageous to provide a soft cantilever probe to overcome the limits [13].

1.2 Polymer-based AFM cantilever probe

A polymeric bead or colloid can be manually attached to a tip-less Si-based cantilever to achieve a partially-polymer-based AFM probe [14]-[17]. However, this assembly method would not only reduce the nanometer- or atomic-scale spatial resolution of AFM, i.e., measure a feature seemingly larger than the actual size or incapable of distinguishing adjacent features while imaging and discerning responses of closely-spaced parts of a cell to external mechanical stimuli, because the radius of a bead/colloid (> 1 μm) is typically > 100 times larger than that of a conventional Si-based tip, but also be inapplicable for a low-cost parallel microfabrication process due to the sequential bead attachment process [14]-[17]. Also, such beads tend to possess a short lifetime due to aging processes such as wear and fatigue after repeated contacts on the sample surface.

Various surface- and bulk-micromachining fabrication processes (e.g., mold-and-transfer technology [18]) that use different kinds of polymers such as SU-8, Polyimide, and Novolak photoresist have been proposed to implement a soft cantilever probe for AFM [18]-[22]. However, they rely on rather sophisticated techniques such as wafer-/chip-scale bonding or bulk Si etching for release and handling of the cantilever probe [18]-[22]. The body of the cantilever needs to be sufficiently thick, which renders it stiffer, in order to avoid undesirable bending caused by strain gradient within the structure. Recently, various surface-micromachining processes have been developed to implement a fully-polymeric AFM probe, yet, with a spring constant well above 1 N/m [19] or with a radius of curvature of the tip well above 100 nm [13], [18].

1.3 Objective and Approach

Micromachined polymer-based AFM probes developed to date still consist of a fairly stiff

cantilever with a relatively high spring constant and a blunt tip, which would damage the cell membrane while high-speed scanning and reduce the accuracy and sensitivity of mechanical measurements (e.g., nanoindentation) on live cells due to large adhesive forces and thus large imaging forces.

In this work, we report a very soft AFM probe, which comprises a polymer-based V-shaped cantilever with a sharp tip at its free end, in order to enable biological research requiring non-destructive, high-speed, high-resolution topographical imaging and nanomechanical characterizations of sub-cellular and cellular samples. A reliable three-mask surface-micromachining process that incorporates a low-cost assembly method and bio-compatible materials is developed to implement polymer-based V-shaped prototype cantilever probes. The physical properties of fabricated prototypes such as effective spring constant, resonant frequency, and quality factor are determined experimentally via thermal noise method and analytically via finite element and parallel-beam approximation methods.

One of the fabricated V-shaped cantilever probes and a commercial Si_3N_4 cantilever probe are employed for nanoindentation measurements of live mammalian cells (human cervical epithelial cancer cells, called “HeLa”) in liquid, and experimental results are compared against each other. It is seen that deformation and/or distortion of the cell membrane is reduced significantly when the polymer probe is used.

For further AFM-based biological studies, the design and fabrication process of the prototype probe are fine-tuned. First, we achieve a low effective spring constant of ~0.01 N/m, which is over an order of magnitude smaller than that of a typical Si-based AFM probe, by employing an acrylic polymer as a structural material. Second, we achieve a sharp probe with a radius of curvature as small as ~40 nm, which is comparable to that of a typical Si-based AFM probe, via sequential depositions of low- and high-viscosity acrylic polymers. Third, we achieve a

reasonably straight cantilever with a strain gradient as low as 10^{-4} μm^{-1} via proper design of the optical reflection coating, i.e., via corrugating the coating or confining it to the tip region.

1.4 Organization of Thesis

The thesis is organized as follows: Chapter 2 discusses the proposed polymer-based AFM probe from design, fabrication, to characterization. Experimental and analytical values including spring constant, resonant frequency, and quality factor are obtained using thermal noise method, finite element method, and parallel beam approximation method. Chapter 3 presents the results of experimental evaluation with nanoindentation using both fabricated V-shaped polymer-based cantilever probe and a commercial Si_3N_4 cantilever probe. Enlightened by the results, fine-tuned design of polymer-based probe is shown in Chapter 4 with characterization of tip sharpness, strain gradient, and spring constant. Finally, in Chapter 5, the thesis is concluded summarizing all the findings.

Chapter 2

PROPOSED POLYMER-BASED AFM CANTILEVER PROBE

2.1 Design and structure

Fig. 2.1 shows an isometric schematic, design parameters and values, and scanning electron micrographs (SEMs) of polymer-based triangular and rectangular cantilever probes. Fabricated V-shaped and rectangular prototype cantilever probes were integrated into the piezoelectric actuator of a commercial AFM system (Bruker Corp., Dimension Icon®).

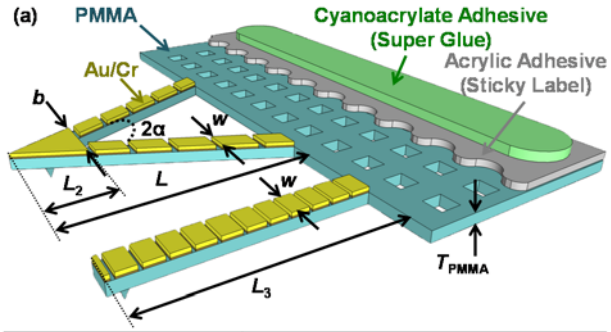

(b) Parameter	Value
L	100, 150, 200, 250, 300 µm
L_2	60 µm
L_3	40, 60, 80, 100, 120, 140, 160 µm
$b = 2 \cdot w$	40 µm
$T_{Au} = 7 \cdot T_{Cr}$	70 nm
T_{PMMA}	2.5 µm

Fig. 2.1 (a) Isometric view of V-shaped and rectangular polymer-based cantilever probes. (b) Design parameters and values.

A low-cost three-mask process was developed to fabricate the polymer-based V-shaped and rectangular cantilevers (in Fig. 2.1) for AFM nanoindentation on live mammalian cells in liquid. Bio-compatible materials—Poly(Methyl MethAcrylate) (PMMA) [23] and Au/Cr [24] were used for the body/anchor and reflective coating of the cantilevers, respectively; Cyanoacrylate adhesive [25] (Loctite® super glue) and Acrylic emulsion-based permanent adhesive [26] (Avery®

6737) were attached on the anchor of the cantilever array (Fig. 2.1(a)).

2.2 Fabrication Process

A Si die (~2 cm × ~2 cm) was used to fabricate cantilever arrays. A single die contains ten arrays. Each array possesses one anchor, which is shared by V-shaped cantilevers of five different lengths or rectangular cantilevers of six different lengths. Fig. 2.2 shows cross-sections of the fabrication process flow. The process begins with wet thermal oxidation with a mixture of H_2O vapor and O_2 at 1140 °C for 20 min, to grow 250 nm Silicon Dioxide (SiO_2) on the Si substrate. The oxide layer was patterned by photolithography and removed by 30:1 buffered oxide etch (BOE) to form square holes (25, 49, 100, and 225 μm^2), which serves as a hardmask for the subsequent anisotropic wet etching of Si. The substrate was then immersed in an etchant comprising 250 ml KOH, 200 ml 2-propanol, and 800 ml H_2O and agitated at 75 °C for 17 min to produce an inverted pyramidal pit as shown in Fig. 2.2(a); KOH etches Si more quickly in the <100> and <110> directions than in the <111> direction and hence exposes (111) planes to form the sidewalls of the pit. The oxide hardmask was removed in 30:1 BOE. 200 nm wet SiO_2 was then grown at 1140 °C for 18 min (Fig. 2.2(b)), which serves as a sacrificial layer and as a mold for the formation of a polymer probe. Because local oxidation rate near the bottom of the concave pyramidal pit is slower than that on the other exposed surfaces due to less surface areas available (in order for oxidants to react with Si at the Si/SiO_2 interface), a sharp probe tip with a radius of curvature as small as 10 nm can be achieved [27]. A 2.5 μm PMMA layer (MicroChem Corp. 950PMMA [28]) was spin-coated at 2000 rpm and hard-baked at 140 °C for 3 min, followed by electron-beam evaporation and patterning of a 10 nm Cr adhesion layer and a 70 nm Au reflection layer. Using the Au/Cr layers as a hardmask, the PMMA layer was etched in O_2 plasma at 303 °K and 50 mT with 200 W of RF power for 15 min (Fig. 2.2(c)). The Au/Cr reflective coating was

then patterned by photolithography and etched using Au/Cr etchants to produce a corrugated surface, Au/Cr/PMMA ridges and PMMA valleys as shown in Fig. 2.2(d). The distance between the ridges and valleys was designed to be 2 μm, which is the minimum feature size that can be resolved by the contact printer used for this work. The width and length of Au and Cr at the tip region were designed to be greater than 20 μm in order to reflect the laser light to the photodetector and hence track the cantilever motion.

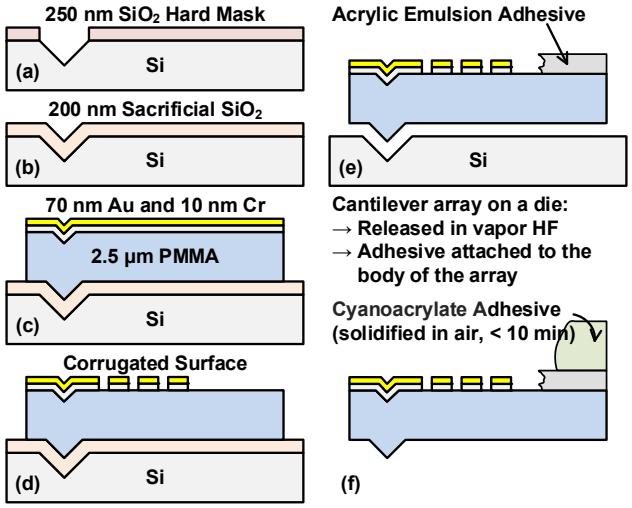

Fig. 2.2 A low-cost three-mask surface-micromachining process: (a) Mask 1: Formation of a pyramidal pit through Si wet etching using an oxide as a hard mask. (b) Deposition of a sacrificial oxide. (c) Spin-coating of PMMA, followed by electron-beam evaporation of Cr and Au. Mask 2: Patterning and etching of Au/Cr/PMMA. (d) Mask 3: Formation of a corrugated reflective coating by patterning and etching of Au/Cr. (e) Release of a cantilever array in vapor HF. (f) Cyanoacrylate adhesive applied to stiffen the anchor of the array.

The corrugation pattern is to relieve residual stresses within the films and hence achieve relatively flat cantilever surfaces. It should be noted that, during the evaporation of Au and Cr, the kinetic energy of the metal atoms is transferred to PMMA as heat. As a result, the underlying PMMA layer is expanded to fit Au/Cr, i.e., PMMA is under tensile stress as the thermal expansion coefficient of PMMA ($70 \cdot 10^{-6}$ K^{-1} [29]) is larger than that of Au and Cr ($14.2 \cdot 10^{-6}$ K^{-1} [30] and $6.2 \cdot 10^{-6}$ K^{-1} [30], respectively). Due to the stress gradient created within the films, PMMA tends to shrink more than Au/Cr, resulting in a severe bending of the released cantilever. The undesirable strain gradient was reduced by half by relieving the residual stresses locally via corrugation of Au/Cr (Figs. 2.3(a) and 2.3(b)). The strain gradient of the fabricated cantilever

before *versus* after corrugation was ~4.0×10^{-3} μm^{-1} *versus* ~2.0×10^{-3} μm^{-1}, respectively. However the cantilever still bent up and it was hard to reflect laser back to photodiode detector in the correct direction.

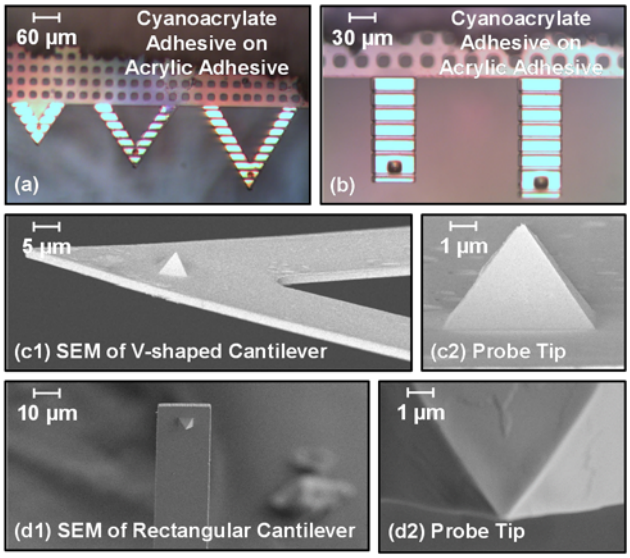

Fig. 2.3 (a) and (b) Plan-view micrographs of fabricated V-shaped and rectangular cantilever arrays, respectively. (c) SEMs of a fabricated V-shaped cantilever probe. (d) SEMs of a fabricated rectangular cantilever probe.

A low-cost method requiring neither anisotropic bulk Si etching for release [18]-[20] nor wafer-/chip-scale bonding for handling [20]-[22] was developed to detach cantilever arrays from the substrate (Figs. 2.2(e) and 2.2(f)). After the fabricated die was released in HF/H_2O vapor (49 % HF) at 45 °C for an hour, each array on the die was lifted up sequentially using the adhesives as a handle. Specifically, approximately 60-μm-thick Acrylic emulsion-based permanent adhesive was attached onto the anchor of the array. To stiffen the anchor of the array and hence prevent the anchor from fluctuating in liquid during nanoindentation tests, extra > 200 μm Cyanoacrylate adhesive (Fig. 2.2(f)) was coated atop the Acrylic adhesive. Using the adhesives as a handle, the array was lifted up from the substrate; No stiction was observed between the PMMA-based array and the Si substrate. Each detached cantilever array was then installed into the AFM system. Albeit low-cost, simple, and easy, the proposed assembly method might not be suitable for high-volume manufacturing since the imprecise manual attachment of the adhesives onto the anchor

would cause misalignment and hence device-to-device variability; Yet, it would be adequate for low-cost rapid prototyping of soft cantilever probes for use in laboratories for biological studies.

2.3 Characterization

The mechanical properties of the fabricated V-shaped and rectangular PMMA-based cantilever with the corrugated optical coating are obtained via experimental measurements, finite element simulations, and analytic calculations. A fabricated array that comprises cantilevers of five different lengths is installed into the piezoelectric positioner of a commercial AFM system (Dimension Icon®, Bruker Corp.), as illustrated in Fig. 2.4. The actuator was driven by a triangle input signal to position the prototype relative to a live cell in a liquid culture medium. A photodetector array collects the laser reflected back from the surface of the cantilever in order to measure probe-cell interaction forces and hence cantilever deflections when the probe touches and indents the cell surface. A decrease in cantilever deflection indicates the indentation of the cell membrane.

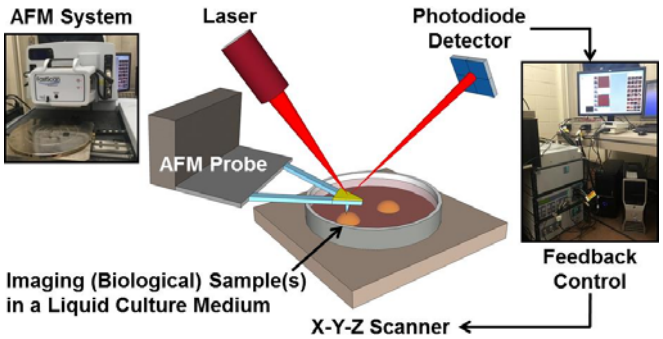

Fig. 2.4 Simplified schematic of the AFM system setup used for this work.

2.3.1 Thermal Noise Method

The physical characteristics of fabricated triangular and rectangular cantilevers including effective spring constant (k_{eff}), resonant frequency (f_{res}), and quality factor (Q) were determined

using analytic equations, finite element simulations [31], and thermal noise analysis. For thermal noise analysis, a laser beam was shone onto the tip region of the cantilever probe, and the reflected laser signal was collected by a photodiode array. The reflected signal fluctuates continuously over time due to the thermally-induced vibration of the cantilever. The resulting time-domain function was transformed into the power spectral density (in Fig. 2.5) by the AFM system.

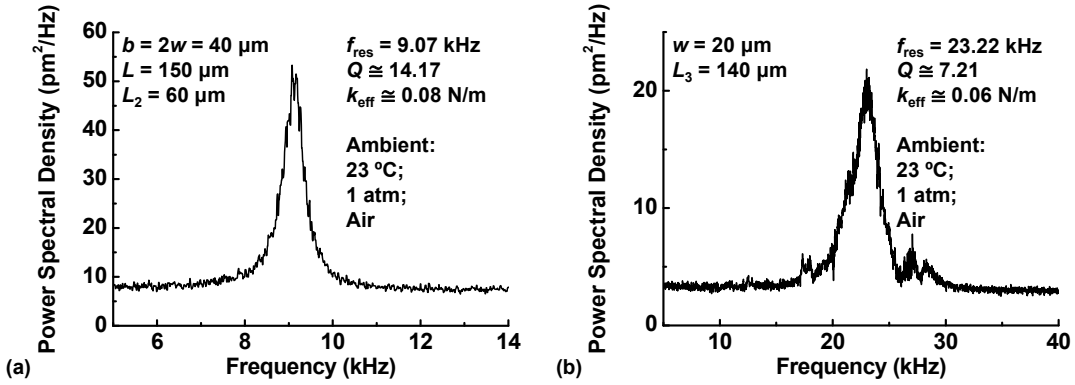

Fig. 2.5 Measured thermal noise frequency spectrum of fabricated PMMA-based (a) V-shaped and (b) rectangular cantilever probes, showing the resonance peak. A Lorentzian function was fitted to the spectrum to extract k_{eff} values.

Measured thermal fluctuations of fabricated V-shaped and rectangular cantilevers as a function of frequency are shown in Figs. 2.5(a) and 2.5(b), respectively. According to the principle of equipartition of energy, the elastic energy (E_{elastic}) stored in a cantilever at thermal equilibrium due to random vertical movements is equal to the average thermal energy per degree of freedom [32], [33]:

$$E_{\text{elastic}} = \frac{1}{2} k_{\text{eff}} \left\langle x^2 \right\rangle = \frac{1}{2} K_{\text{B}} T$$

where k_{eff} is the effective spring constant of the cantilever, $\langle x^2 \rangle$ is the frequency-dependent mean-square value of the thermal fluctuations, K_{B} is the Boltzmann's constant, and T is the absolute temperature in Kelvin. A Lorentzian function was fitted to the measured frequency spectrum to determine the total E_{elastic} (from the area under the curve) [34]. With measured E_{elastic}

and $\langle x^2 \rangle$, k_{eff} values were extracted using the above equation—k_{eff} of ~0.08 N/m and ~0.06 N/m were obtained for the cantilevers in Figs. 2.5(a) and 2.5(b), respectively.

2.3.2 Finite Element Method

The finite element method (FEM) is a widely-used simulation method in microelectromechanical systems (MEMS) for accurate static and dynamic characterizations of micro structures. It divides a large structure into smaller and simpler parts named finite element. Each volumetric element represents a discrete portion of the physical structure. After combining individual equations of modeling these small parts by common nodes, FEM generates a large mesh to model the entire problem. The number of finite elements per volume, referred as the mesh density, determines the accuracy of simulation as the displacement of each node serves as the fundamental variable in a stress analysis. When the nodal displacements are known, strains and stresses within each finite element can be determined. FEM simulation were performed using CoventorWare® 10 for this work. CoventorWare is an integrated suite of software tools known for its accuracy, speed and capacity to design and simulate real-world MEMS devices. Structures of V-shaped cantilevers were built exactly according to parameters defined in Fig. 2.1(b). Resonant frequency was recorded when the cantilever achieved largest swing. With calculated mass, spring constant was determined under Hooke's law.

2.3.3 Parallel Beam Approximation Method

Analytically, spring constant for rectangular cantilever is commonly calculated [22]:

$$k = \frac{Et^3 w}{4L_3^3}$$

where E is the Young's modulus of PMMA, t is the thickness of cantilever, w is the width, and L_3 is the length of the rectangular cantilever (illustrated in Fig. 2.6).

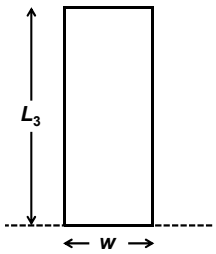

Fig. 2.6 Rectangular AFM cantilever showing length and width. The dashed line is where the clamped boundary condition is applied.

For V-shaped cantilevers, several approaches using parallel beam approximation (PBA) have been reported to evaluate the spring constants [35]-[37]. The V-shaped cantilever can be approximated as two rectangular beams joined in parallel. This "parallel beam approximation" (PBA) was first proposed by Albrecht *et al.* [38], and modified by Butt *et al.* [35] and Sader *et al.* [36]. However, the PBA is a non-unique approximation; could be interpreted into various equations. This is because the oblique-crossing rectangular arms of the V-shaped cantilever are skewed instead of simply being parallel as approximated. Therefore, it creates differences in the choice of an appropriate length and width for the two rectangular arms [37].

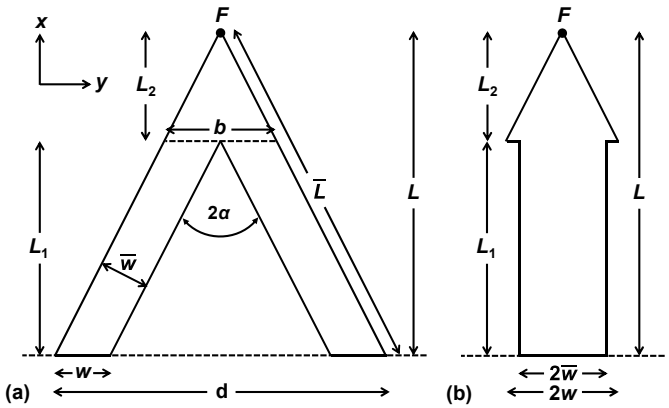

Fig. 2.7 Cross-sectional view of V-shaped AFM cantilever and its equivalent showing dimensions and position of end-tip loading F. The dashed line is where the clamped boundary condition is applied.

The analysis diagram of a V-shaped cantilever is displayed in Fig. 2.7. Based on different selection of the length and width, the equation for the spring constant of a V-shaped cantilever varies. Albrecht *et al.* selected the width and length of their PBA formulation to be $\overline{w}$ and $\overline{L}$. The equation is found to be

$$k_{\text{Albrecht}} = \frac{Et^3 w}{2L^3}\left(1+\frac{d^2}{4L^2}\right)^{-2}$$

Butt *et al.* selected *d* and *L* to be the width and length of the rectangular arms instead. The equation is modified by simply reduplicating the rectangular cantilever spring constant equation, which is

$$k_{\text{Butt}} = \frac{Et^3 w}{2L^3}$$

Sader *et al.* chose the width and length as L_1 and $\overline{w}$, respectively, and their formulation can be shown to result in the following expression for the spring constant

$$k_{\text{Sader}} = \frac{Et^3 w}{2L^3}\cos\alpha\left[1+\frac{4w^3}{d^3}\left(3\cos\theta-2\right)\right]^{-1}$$

Another formulation which completely neglects the anticlastic curvature in the deflection function of the cantilever is the zeroth-order solution of Eq. (A5) of Ref. [38].

$$k_{zero} = \frac{Et^3 d}{2L^3}(1+\frac{4d^3}{b^3})^{-1}$$

where *E* is the Young's modulus of PMMA, *t* is the thickness of cantilever, *w* is the width of skewed rectangular arm for the above four equations. The length of cantilever *L* and angle of skew of the rectangular arm α are also illustrated in Fig. 2.7.

However, cantilever with multi-layers and inhomogeneous thickness couldn't be adapted to the equations directly. We begin by examining in detail the geometry of the V-shaped cantilever illustrated in Fig. 2.1. Adapted in this case, the cantilever consists of two skewed rectangular arms and a triangular end part (Fig. 2.7(a)).

Based on Sader PBA, the original V-shaped cantilever is equivalent to a cantilever which has its skewed rectangular arms replaced by a single unskewed rectangular plate of length L_1 and width $2\overline{w}$ ($\overline{w} = w \cdot \cos\alpha$) as is illustrated in Fig. 2.7(b).

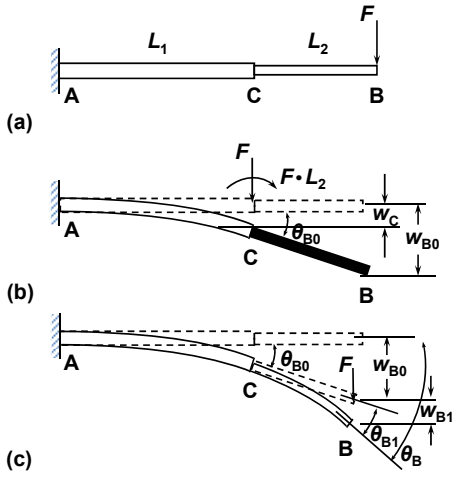

Fig. 2.8 Customized parallel beam approximation by integrating unskewed rectangular plate (A-C) and triangular end part (C-B) separately. Ratio between load force F and deflection w_B was calculated as spring constant k.

Bending momentum $M(x)$ and deflection function $w(x)$ are related to the force F applied at the end as

$$EIw''(x) = M(x) = F(L - x)$$

with boundary condition at the ends of unskewed rectangular plate

$$\begin{cases} EIw'(0) = -\dfrac{1}{2}FL^2 + C_1 \\ EIw(0) = \dfrac{1}{6}FL^3 + C_2 \end{cases}$$

The maximum angle and deflection of a simple rectangular cantilever beam can be obtained when $x = L$.

$$\begin{cases} \theta_{\max} = \dfrac{FL^2}{2EI} \\ w_{\max} = \dfrac{FL^3}{3EI} \end{cases}$$

In our case, with force F applied at the end (Fig. 2.8(a)), we first assume the triangular end part rigid, deflection consists of the bending of unskewed rectangular plate and the angle introduced by it (Fig. 2.8(b)).

$$w_{\mathrm{B0}} = w_{\mathrm{C}} + \theta_{\mathrm{B0}} \cdot L_2$$

where w_{C} and θ_{B0} can be calculated by considering transverse shearing force and angular momentum.

$$\begin{cases} \theta_{\mathrm{B0}} = \dfrac{FL_1^2}{2E_1I_1} + \dfrac{(FL_2)L_1}{E_1I_1} \\ w_{\mathrm{C}} = \dfrac{FL_1^3}{3E_1I_1} + \dfrac{(FL_2)L_1^2}{2E_1I_1} \end{cases}$$

Thus the deflection w_{B0} is

$$w_{\mathrm{B0}} = \frac{F(L_1^3 + 3L_1^2L_2 + 3L_1L_2^2)}{3E_1I_1}$$

where $I_1 = \dfrac{1}{12}(2\overline{w})T_{\mathrm{PMMA}}^3$ is the second moment of area. Secondly, we assume the unskewed rectangular plate is stable and rigid (Fig. 2.8(c)). Deflection of the triangular end part is similar with above and we simply replace second moment of area I_2 with I_2(x) for its dependance on x across variable cross-section.

$$I_2(x) = \frac{1}{12} \cdot 2(L_2 - x)\tan\alpha \cdot T_{\mathrm{Total}}^3$$

where $T_{\text{Total}} = T_{\text{PMMA}} + T_{\text{Cr}} + T_{\text{Au}}$, α is half the angle of two skewed arms in Fig. 2.7(b).

The maximum angle and deflection of a triangular end part beam can be obtained when $x = L_2$.

$$\begin{cases} \theta_{\text{B1}}(x) = \dfrac{6Fx}{E_2 \tan\alpha \cdot T_{\text{Total}}^3} = \dfrac{6FL_2}{E_2 \tan\alpha \cdot T_{\text{Total}}^3} \Big| x = L_2 \\ w_{\text{B1}}(x) = \dfrac{3Fx^2}{E_2 \tan\alpha \cdot T_{\text{Total}}^3} = \dfrac{3FL_2^2}{E_2 \tan\alpha \cdot T_{\text{Total}}^3} \Big| x = L_2 \end{cases}$$

By adding w_{B0} and w_{B1} together, we get the relation between total beam deflection w_{B} and load force F.

$$w_{\text{B}} = \frac{F(L_1^3 + 3L_1^2L_2 + 3L_1L_2^2)}{3E_1I_1} + \frac{3FL_2^2}{E_2 \tan\alpha \cdot T_{\text{Total}}^3}$$

Spring constant $k = F/w_{\text{B}}$ could be easily calculated with given parameters of V-shaped cantilevers defined in Fig. 2.1(b). E_1 is the Young's modulus of PMMA and E_2 is the equivalent elastic modulus, which is the weighted harmonic mean in respect of thickness of the materials Au, Cr, and PMMA [39]:

$$E_2 = \frac{\sum E_{\text{i}} T_{\text{i}}}{\sum T_{\text{i}}}$$

With T_{i} shown in Fig. 2.1(b), E_{PMMA} = 2 GPa [40], E_{Cr} = 279 GPa [41], and E_{Au} = 79 GPa [42], E_2 was calculated to be 4.59 GPa.

Measured k_{eff} values of fabricated V-shaped and rectangular cantilevers were plotted as a function of cantilever length (L) and compared against the calculated and simulated values as shown in Fig. 2.9. All of the experimental, FEM, and analytical values decrease with increasing cantilever length (L and L_3) as expected from (3) and (4). The measured values are consistently smaller than the predicted values independent of L and L_3, for the following reasons: Firstly, the fraction of the anchor of the cantilever array uncoated with the adhesives—the perforated areas in Figs. 2.3(a) and 2.3(b) render the cantilever less stiff and hence lower the experimental k_{eff}. Such process-

induced variations would cause device-to-device variability. Secondly, inaccuracy in the measurements of cantilever dimensions and approximations in material properties contribute to the difference between the measured and predicted values.

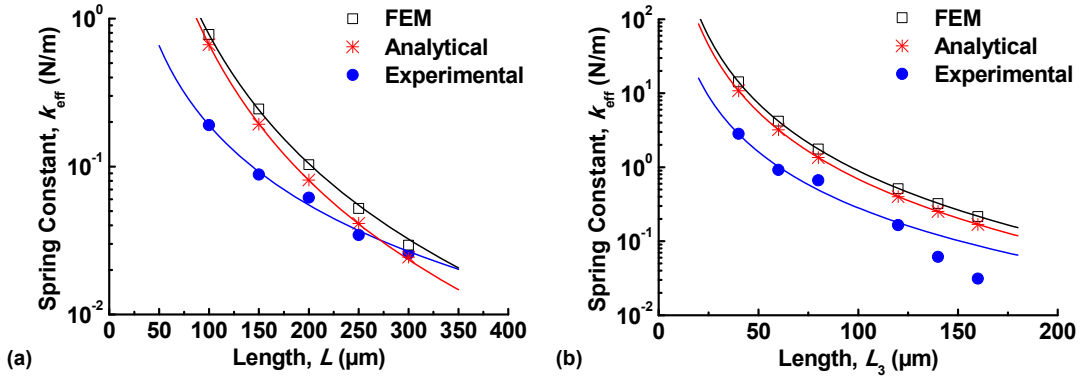

Fig. 2.9 Measured, finite element method (FEM), and analytical k_{eff} values of fabricated (a) V-shaped and (b) rectangular PMMA-based cantilever probes. Measured and predicted k_{eff} decrease with increasing L and L_3 as expected. CoventorWare® 10 was used for the FEM simulation.

Chapter 3

EXPERIMENTAL EVALUATION WITH NANOINDENTATION

3.1 Preparation of Biological Samples

Human cervical epithelial cancer cells—"HeLa" were employed in the AFM nanoindentation tests to evaluate and validate the fabricated prototype cantilever probe. They serve as exemplary mammalian cells that can elicit the mechanical evolution of dynamic cellular processes (e.g., epithelial-mesenchymal transition (EMT), which is a critical biologic process in embryonic development and cancer progression [43]-[44]). HeLa cells were cultured as described previously [45]. Briefly, they were grown in a Dulbecco's Modification of Eagle's Medium (DMEM; Mediatech, Catalog No. 10017CV) containing 10 % fetal bovine serum (Sigma Aldrich, Catalog No. F6178) and 1 % Penicillin/Streptomycin solution (Gibco, Catalog No. 15070063), and they were passaged with Trypsin-Ethylene-Diamine-Tetraacetic-Acid (Trypsin-EDTA) digestion every three days. 1×10^6 HeLa cells (shown in Fig. 3.1) were then seeded into a 60 mm cell culture Petri dish (Thermo Scientific Nunc, Catalog No. 12-565-97) containing 5 ml of fresh complete culture medium and were grown overnight to a complete confluent monolayer.

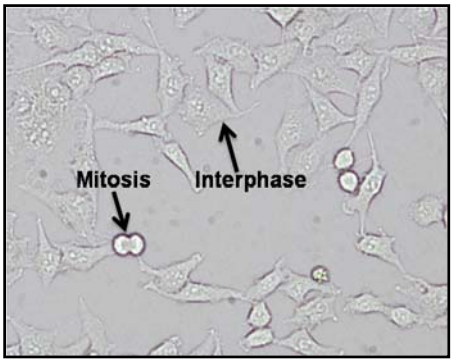

Fig. 3.1 Phase-contrast microscopy of HeLa cells (15×).

3.2 Experimental Setup and Method

A fabricated PMMA-based V-shaped cantilever probes (with $k_{eff} \cong 0.08$ N/m) was employed in the AFM nanoindentation measurements of live HeLa cells (in Fig. 3.1) in a liquid culture medium using the testing setup (illustrated in Fig. 3.2). Measurement results were compared against those obtained using a commercial Si_3N_4 V-shaped cantilever probe with $k_{eff} = 0.06$ N/m (Bruker Corp., Model MLCT).

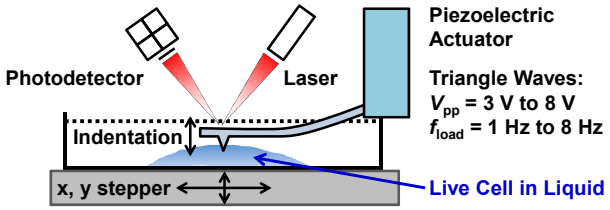

Fig. 3.2 Experimental setup for AFM nanoindentation on live cells in liquid.

3.3 Nanoindentation Results

Nanoindentation measurements were conducted by acquiring AFM force-distance curves continuously over time. For the measurements, a triangle input voltage signal (with respect to time) with a fixed amplitude (V_{pp}) and a constant force load rate (f_{load}) was applied to drive the piezoelectric actuator of the AFM system (shown in Fig. 3.2) so that the cantilever probe can contact, indent, and retract from the cell membrane. Probe-cell interaction forces were measured via cantilever deflections at different V_{pp} and f_{load}. Six different voltage amplitudes (V_{pp} from 3 V to 8 V with one volt increment) and eight different force load rates (f_{load} from 1 Hz to 8 Hz with 1 Hz increment) were applied.

During the continuous measurements, the force exerted on the cell can deform and/or distort the cell membrane when the cantilever probe is stiff and hard. This distortion-induced fracture of the cell membrane is signaled by a dramatic drop in probe-cell interaction force (F_{int})—due to the

significant loss of elasticity of the cell membrane. Thus, the time taken for F_{int} to decrease by 50 %, i.e., time to $0.5F_{int}$, can be used as a figure-of-merit to quantify the practical contact stiffness of the probe.

Figs. 3.3 and 3.4 show measured probe-cell interaction forces *versus* time using the PMMA- and Si_3N_4-based probe, each driven with V_{pp} = 3 V and f_{load} = 1 Hz and 8 Hz. When the Si_3N_4 probe was used, F_{int} dropped abruptly in less than 100 seconds as shown in Figs. 3.3(a) and 3.4(a). This change in F_{int} indicates that a significant destruction of the cell membrane has occurred since the probe poked into the cell membrane. In contrast, when the polymer probe was used, deformation and distortion of the cell membrane was reduced significantly; very minimal or no damage was observed even after repetitive indentations for ≥ 2000 seconds as shown in Figs. 3.3(b) and 3.4(b). (Due to the equipment limit, all measurements performed with the polymer probe were taken only up to 2000 seconds.) It should be noted, firstly that, although a used Si_3N_4 cantilever probe with a relatively-dull worn-off tip (with a radius of < ~100 nm) was purposely used in this work, because the Si_3N_4 probe tip is still sharper than the polymer probe tip (with a radius of < ~150 nm as shown in Fig. 2.3), the Si_3N_4 probe would exert a relatively larger force on the cell membrane than the prototype probe. On the other hand, given the same indentation depth, the Si_3N_4 probe would exert less force on the membrane than the polymer probe since it possesses a slightly lower k_{eff} of 0.06 N/m (*vs.* 0.08 N/m). Qualitatively, the two effects (due to the tip sharpness and spring constant) would offset each other to some degree and might minimally influence the results. Secondly, the findings in Figs. 3.3 and 3.4 would be because contact stiffness is lower for the PMMA probe than for the Si_3N_4 probe since Young's modulus and hardness of PMMA ($E \cong 2$ GPa [40] and $H \cong 0.4$ GPa [46], respectively) are lower by two orders of magnitude than those of Si_3N_4 ($E \cong 310$ GPa [47] and $H \cong 50$ GPa [48], respectively).

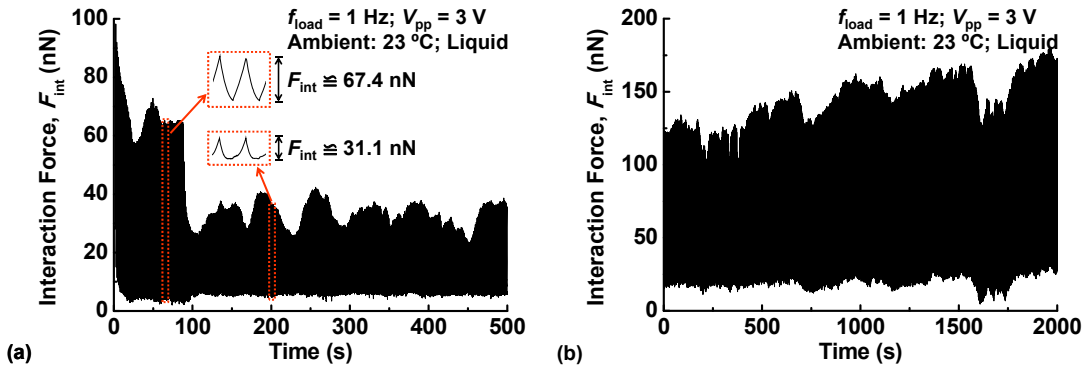

Fig. 3.3 Measured interaction forces F_{int} between a probe and a HeLa cell using: (a) Si_3N_4 probe with V_{pp} = 3 V and f_{load} = 1 Hz; (b) PMMA-based probe with V_{pp} = 3 V and f_{load} = 1 Hz.

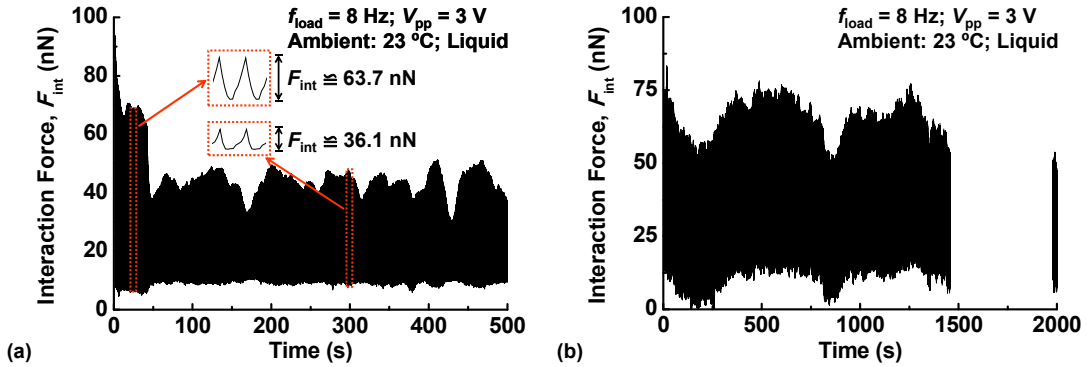

Fig. 3.4 Measured interaction forces F_{int} between a probe and a HeLa cell using: (a) Si_3N_4 probe with V_{pp} = 3 V and f_{load} = 8 Hz; (b) PMMA-based probe with V_{pp} = 3 V and f_{load} = 8 Hz.

The improvement, i.e., a significant reduction in damage to the cell membrane, was quantified by measuring the time to $0.5F_{int}$ at different f_{load} and V_{pp} values using both polymer and Si_3N_4 probes. Fig. 3.5 shows that the time to $0.5F_{int}$ decreased gradually with increasing f_{load} when the Si_3N_4 probe was used. This decrease would be because the acceleration at the peak of the input triangle wave (with V_{pp} = 3 V) and hence the maximum applied force increases with increasing f_{load}. Similarly, the time to $0.5F_{int}$ decreased consistently with increasing V_{pp} (Fig. 3.6). As V_{pp} increases, both indentation depth and force load applied to the cell surface increase, causing larger deformation and/or distortion of the cell membrane. In contrast, when the polymer probe was used, the amplitudes of F_{int} remained at constant values for a much longer time (> 2000 s) independent of f_{load} and V_{pp} (Figs. 3.5 and 3.6). No degradation in F_{int} was observed even after few rounds of the 2000-second-measurements for all f_{load} and V_{pp}.

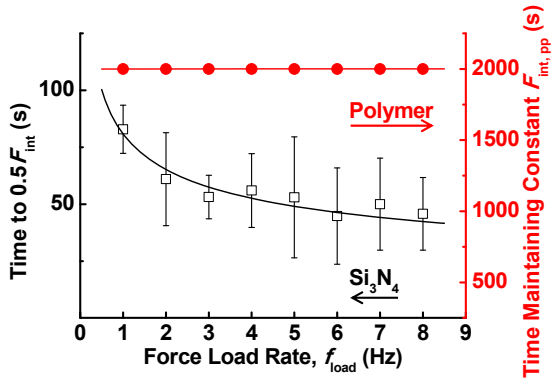

Fig. 3.5 Measured time to half F_{int} *vs.* force load rate, f_{load} using the polymer probe (right) and Si_3N_4 probe (left) in liquid at 23 °C with V_{pp} = 3 V.

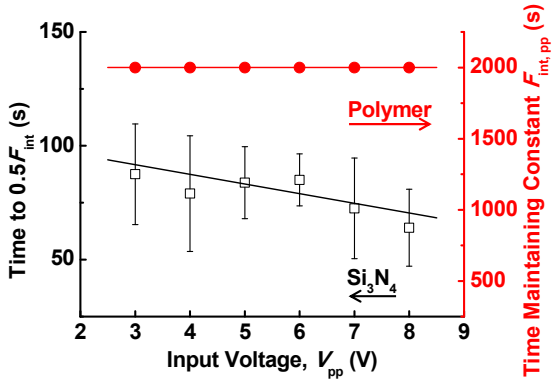

Fig. 3.6 Measured time to half F_{int} *vs.* peak-to-peak input voltage, V_{pp} using the polymer probe (right) and Si_3N_4 probe (left) in liquid at 23 °C with f_{load} = 1 Hz.

Chapter 4

FINE-TUNED PMMA-BASED CANTILEVER PROBE

4.1 Design and Fabrication

Fig. 4.1 presents an isometric schematic and design parameters and values of the AFM probes of this work, each consisting of a polymer-based cantilever with a tip near its free end. The conventional V-shaped structure is employed to minimize the undesirable effect of torsional and/or lateral bending on image quality [49]—particularly for contact-mode AFM in a liquid medium, which is the cell culture primarily used for biological research due to nutrient contents. The optical reflection coating, Gold (Au) atop Chromium (Cr) of the cantilever shown at the bottom of Fig. 4.1(a) is corrugated to form crests and valleys, and that of the other cantilever (in Fig. 4.1(a)) covers the tip region only, in order to examine the effect of corrugation on achieving a flat cantilever structure.

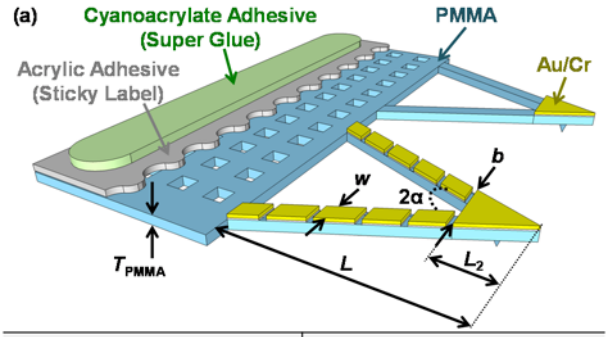

(b) Parameter	Value
L	200, 250, 300, 350, 400 μm
L_2	80, 85, 90, 95, 100 μm
$b = 2 \cdot w$	80 μm
T_{Au}	50, 70, 90 nm
T_{Cr}	10 nm
T_{PMMA}	2.5 μm
E_{cr}	279 Gpa
E_{Au}	79 Gpa
E_{PMMA}	2 GPa

Fig. 4.1 (a) Three-dimensional view of PMMA-based V-shaped AFM probes. (b) Design parameters and values.

Fig. 4.2 shows a three-mask surface-micromachining process flow developed to implement the cantilever design in Fig. 4.1. This process is identical to that reported previously [18], [50] except that a bi-layer resist comprising Poly(MethylMethAcrylate) (PMMA) with different molecular weights and viscosity values is used to attain a sharp tip and provide mechanical support. Briefly, the process begins with the deposition of a thermal wet Silicon Dioxide (SiO_2), which serves as a hardmask in the subsequent Si wet etching for the formation of an inverted pyramidal pit on the Si substrate (Fig. 4.2(a)). After growing another wet SiO_2, which acts as a sacrificial layer (for the separation of fabricated cantilever arrays from the substrate later in the release step), a bi-layer PMMA resist, a Cr adhesion film, and an Au reflection layer are deposited sequentially and then patterned together for the cross-section in Fig. 4.2(c). Afterward, the Au/Cr optical coating is removed selectively to produce a corrugated pattern (Fig. 4.2(d)) or to leave it only at the tip region (Fig. 4.1(a)), so as to achieve a relatively-flat cantilever surface. The as-fabricated distance between the two crests (pitch) of the corrugated pattern is set to 2 μm, which is the resolution achievable with the contact aligner used for this work. Lastly, fabricated cantilever arrays are freed in hydrofluoric vapor (HF in H_2O), and each array is then detached using commercial adhesives to be integrated into an AFM system (Fig. 4.2(f)). The anchor of the cantilever array is perforated (Fig. 4.1(a)) to facilitate the final release step. Bio-compatible materials: PMMA, Au, Cr, and adhesives [23], [24] are employed for application of the probes in biological studies. Fig. 4.2(i1) shows the plan-view photomicrographs of fabricated cantilever arrays, and Fig. 4.2(i2) presents the isometric- and magnified-view scanning electron micrographs (SEMs) of a fabricated cantilever. The following sub-sections focus on the methods of achieving a sharp polymer-based tip and a relatively flat cantilever surface.

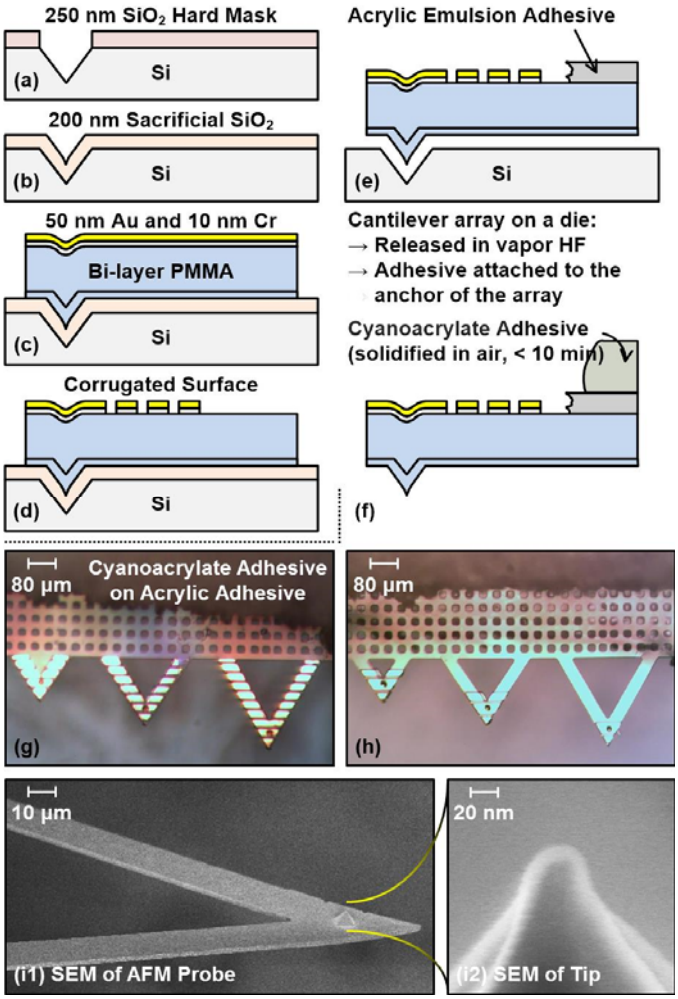

Fig. 4.2 (a)-(f) Surface-micromachining process flow used to fabricate the AFM probes (in Fig. 1). Plan-view photographs of a fabricated cantilever array with (g) Au/Cr corrugated and (h) only at the tip region. (i1) Isometric- and (i2) magnified-view SEM of a fabricated cantilever.

4.2 Implementation

4.2.1 Sharpness of Probe

In contact-mode AFM, tip-sample interaction forces such as friction and adhesive attractive forces determine the quality of topographical images [51]. Particularly, minimization of the adhesive force (F_{ad}) between a tip and a sample is necessary—not only to achieve high-resolution imaging, but also to reduce damage to the tip and the sample and avoid the creation of artifacts

[52]. It has been shown that, the sharper the tip, i.e., the smaller the radius of curvature of the tip, and the lower the adhesive force; Both Derjaguin-Muller-Toporov (DMT) and Johnson-Kendall-Roberts (JKR) theories approximate that F_{ad} between a spherical tip and a flat sample surface is proportional to the radius of the tip [7]:

Table 4.1 Adhesion force F_{ad} for a spherical tip on a flat surface.

	Hertz	DMT	JKR
F_{ad}	0	$2\pi RW$	$\frac{3\pi RW}{2}$

where R is the tip radius, and W is the adhesion work per area. For this reason, commercial Si-based AFM probes require a sharp tip with a radius of curvature of < 50 nm typically [53].

To realize a sharp polymer-based tip, a bi-layer PMMA resist is employed for the structure of this work as shown in Fig. 4.2(c). After the formation of an inverted pyramidal pit and deposition of a sacrificial oxide (Figs. 4.2(a)-4.2(b)), a relatively thin 100 nm PMMA layer with a molecular weight of 495 kDa and a different viscosity value—ranging from 1.5 to 526 cP as tabulated in Table 4.2—is spin-coated to fill the pyramidal cavity. A solvent, Methoxybenzene (known as Anisole), which serves as an organic precursor for synthetic polymers, is used to vary the viscosity values (in Table 4.2), i.e., Anisole came premixed with a different PMMA content: from 2 to 11 % to achieve the values from 7 to 526 cP (MicroChem Corp.[28], [54]). For the viscosity values of 1.5 and 2.9 cP, which correspond to 0.5 and 1 % PMMA in Anisole, respectively, the commercial 2 % PMMA compound is diluted further with a pure Anisole solution (> 99 %, Sigma-Aldrich). Afterward, a 2.5-μm-thick PMMA layer with a molecular weight of 950 kDa and a relatively high viscosity value of 3180 cP is deposited to provide structural support.

Table 4.2 Viscosity values of various PMMA compounds.

PMMA (Molecular Weight in kDa)	PMMA (in %) in Anisole (> 99 %)	Dynamic Viscosity (μ in cP)
PMMA (495)	0.5	1.50
PMMA (495)	1	2.94
PMMA (495)	2	6.97
PMMA (495)	4	23.2
PMMA (495)	6	65.9
PMMA (495)	8	153.8
PMMA (495)	11	525.6
PMMA (950)	11	3180

The tip region of each fabricated AFM probe is scrutinized using the SEM. Fig. 4.3 shows measured radii of curvature of the tip as a function of the PMMA solids content of the first low-viscosity PMMA layer. As the viscosity (μ) increases, i.e., as the PMMA content in Anisole increases, the radius of curvature of the tip increases, i.e., the tip turns out to be blunter, as the spin-deposited molecules are being crammed into the apex of the pit on the Si substrate. This can be explained using the Reynolds number (*Re*), which is inversely proportional to the dynamic viscosity of a fluid [55]; When a PMMA fluid with a smaller *Re* moves relative to the surface of the substrate, the fluid is subject to a larger tangential shear stress ($\tau \propto \mu$ [56]), i.e., it experiences a larger friction force due to a larger viscosity.

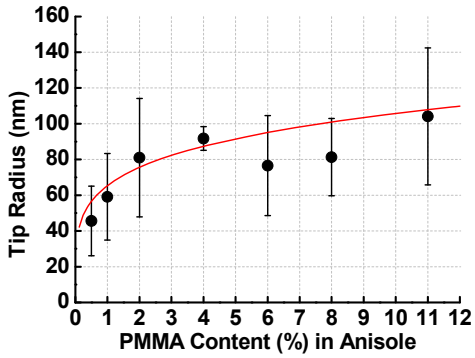

Fig. 4.3 Measured radii of curvature of the fabricated AFM probes as a function of the PMMA solids content in Anisole.

4.2.2 Strain Gradient of Cantilever

An AFM probe requires a reasonably straight cantilever for precise nano- or atomic-scale

imaging and analysis of surface topography; measuring the cantilever deflection (by processing the laser signals bouncing back from the cantilever surface while scanning a sample surface) results in topographic images and tip-sample interaction forces.

When the Au/Cr optical reflection coating is deposited on the PMMA structure, the metal and polymer layers are subject to thermally-induced deformations. Specifically, when evaporated Cr atoms collide with the PMMA surface, the kinetic energy associated with the collision is converted to thermal and elastic energies [57]. The transfer of heat between Cr and PMMA occurs, and the underlying PMMA is extended (i.e., PMMA is under tensile stress) to fit the Cr layer because of the mismatch in the coefficients of thermal expansion (CTEs). Thus, the PMMA layer of the released cantilever tends to shrink, causing a severe out-of-plane deflection (Fig. 4.4(a)). Quantitatively, the bending behavior can be analyzed by calculating the thermal-mismatch stress developed within an as-deposited film. An in-plane biaxial thermal-mismatch stress (σ_{mismatch}) is induced in a film due to a thermal mismatch strain ($\varepsilon_{\text{mismatch}}$) [58]:

$$\sigma_{\text{mismatch}} = \left(\frac{E}{1-\nu}\right)\cdot\varepsilon_{\text{mismatch}} = \left(\frac{E}{1-\nu}\right)\cdot\left(\alpha_{\text{f}}-\alpha_{\text{s}}\right)\cdot\Delta T$$

where E is the Young's modulus, ν is the Poisson's ratio, and $\varepsilon_{\text{mismatch}}$ is the thermal mismatch strain, α_{f} is the CTE of the deposited film, α_{s} is the CTE of the substrate, and ΔT is the difference between the deposition and room temperatures. First, the deposition of PMMA on SiO_2 (Fig. 4.2(c)) induces a tensile σ_{mismatch} of 9.9 MPa in PMMA. E_{PMMA} = 2 GPa, ν_{PMMA} = 0.4, $\alpha_{\text{f}} = \alpha_{\text{PMMA}} = 70\cdot10^{-6}$ /K, and $\alpha_{\text{s}} = \alpha_{\text{OX}} = 0.65\cdot10^{-6}$ /K [29], [40], [59] are used for the calculation. Second, the deposition of Cr on PMMA—E_{Cr} = 279 GPa, ν_{Cr} = 0.21, and $\alpha_{\text{f}} = \alpha_{\text{Cr}} = 6.2\cdot10^{-6}$ /K [60], [61]—causes a compressive σ_{mismatch} of –21.5 GPa within Cr. Similarly, the deposition of Au on the Cr/PMMA substrate—E_{Au} = 79 GPa, ν_{Au} = 0.44, $\alpha_{\text{f}} = \alpha_{\text{Au}} = 14.2\cdot10^{-6}$ /K [60], [61]—results in a compressive σ_{mismatch} of –2.6 GPa in Au; In this case, $\alpha_{\text{s}} = \alpha_{\text{PMMA}} = 70\cdot10^{-6}$ /K is used to approximate the effective CTE of the Cr/PMMA composite [62]. Thus, a stress gradient is created

within the as-deposited films due to $\sigma_{mismatch}$, and the stress gradient is converted into a strain gradient upon release of the cantilever, resulting in out-of-plane bending in Fig. 4.4(a), i.e., the tensile PMMA tends to shrink since it was extended to fit, and the compressive Au and Cr tend to extend since they were compressed to fit.

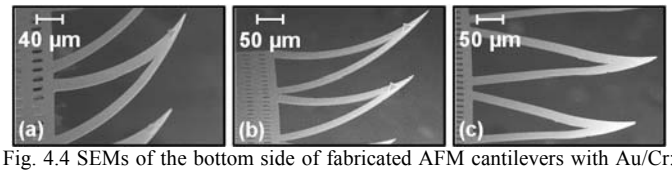

Fig. 4.4 SEMs of the bottom side of fabricated AFM cantilevers with Au/Cr: (a) fully covering the top surface of the cantilever; (b) being corrugated; (c) covering the tip region only.

In order to reduce the strain gradient, the reflection coating is corrugated or added only at the tip region as shown in Figs. 4.1(a), 4.2(g), and 4.2(h). It has been shown that the introduction of such a pattern can locally reduce the residual stress within a film (by a factor of > 10^3 for a single crystal Si for example) [63], [64] and hence relieve the stress/strain gradient within multiple films. The strain gradient is given by [65]:

$$\rho^{-1} = 2 \cdot \Delta z \cdot L^{-2},$$

where ρ is the radius of the curvature, Δz is the out-of-plane deflection of the tip, and L is the cantilever length. Fig. 4.5 plots calculated strain gradients based on measured cantilever deflections (Fig. 4.4) versus cantilever length (L) for different Au/Cr coverage: First, when the top surface of the cantilever is fully covered with Au/Cr, the freed cantilever is deformed dramatically, showing a large strain gradient close to 10^{-2} μm^{-1} (Fig. 4.4(a)); Second, when Au/Cr is corrugated (Fig. 4.1(a) and 4.2(g)), the strain gradient is reduced by > 50 %, yet, still well above 10^{-3} μm^{-1}, and the cantilever is still bent by an unacceptable amount (Fig. 4.4(b)); Third, when Au/Cr covers the tip region of the cantilever only (Figs. 4.1(a) and 4.2(h)), the strain gradient is reduced by about an order of magnitude, close to 10^{-4} μm^{-1}, and the cantilever shows much less deformation (Fig. 4.4(c)).

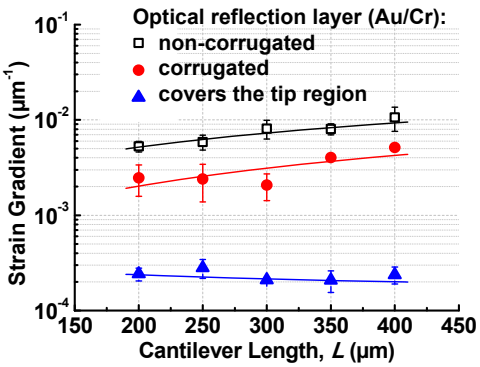

Fig. 4.5 Measured strain gradients versus the cantilever length (L in Fig. 4.1).

4.3 Characterization

In this section, the mechanical properties of the fabricated polymer-based cantilever with the optical coating only at the tip region are examined via experimental measurements, analytic calculations, and finite element simulations. A fabricated array that comprises cantilevers of five different lengths is installed into the piezoelectric positioner of a commercial AFM system (Dimension Icon®, Bruker Corp.), as illustrated in Fig. 2.4. A position-sensitive photodiode detector of the AFM system collects and processes the incident laser light reflected off the surface of the cantilever to detect the deflection of the cantilever, and a feedback loop controls the position of the tip relative to the sample surface while scanning, to maintain a constant probe-sample force and hence image surface features accurately.

The free-end of an AFM cantilever, in the absence of any driving force, is subject to thermally-induced vibrations, due to the random motion of the atoms/molecules composing the cantilever. In equilibrium, the average thermal energy is given by $0.5K_BT$ for the vertical degree of freedom of the cantilever, where K_B is the Boltzmann's constant, and T is the absolute temperature. The theorem of equipartition of energy requires that the thermal energy be equal to the stored elastic energy ($E_{elastic}$) of the randomly-fluctuating cantilever [33]:

$$\frac{1}{2}K_{\mathrm{B}}T = E_{\mathrm{elas}} = \frac{1}{2}k_{\mathrm{eff}}\left\langle x^2\right\rangle \leftrightarrow k_{\mathrm{eff}} = \frac{K_{\mathrm{B}}T}{\left\langle x^2\right\rangle}$$

where k_{eff} is the effective spring constant, and $\langle x^2 \rangle$ is the mean-square value of the thermal fluctuations of the cantilever. At a given temperature, the larger the amplitude of the thermal fluctuations, the smaller the k_{eff}. Methodologically, the time-domain mechanical response of the cantilever to thermal noise (thermal fluctuations versus time) can be measured using the AFM system. This measurement is then translated into the frequency spectrum (power spectral density versus frequency as shown in Fig. 4.6), and a Lorentzian line shape function is fitted onto the measured frequency spectrum to determine the E_{elastic} (from the area under the function) and hence extract the k_{eff} value of the cantilever using above equation: k_{eff} of ~0.029 N/m for the cantilever in Fig. 4.6.

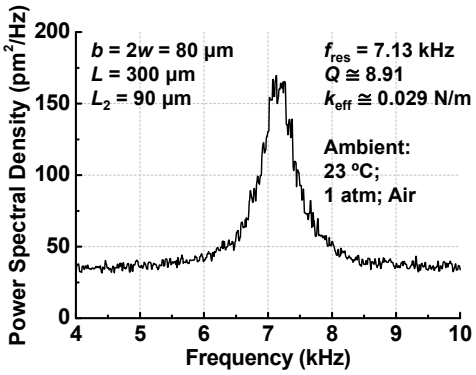

Fig. 4.6 Measured thermal noise frequency spectrum of a fabricated PMMA-based AFM cantilever.

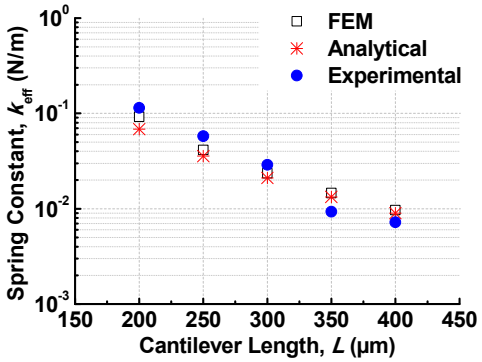

Fig. 4.7 Experimental, analytical, and simulated k_{eff} values of fabricated PMMA-based AFM cantilevers.

The experimental, calculated, and simulated k_{eff} values of fabricated cantilevers as a function of cantilever length are plotted in Fig. 4.7. These values decrease with increasing L as well predicted by the conventional parallel beam approximation method [37]:

$$k_{\text{eff}} = \frac{E_{\text{PMMA}} \cdot t^3 w}{2L^3} \cos\alpha \left\{ 1 + \frac{4w^3}{d^3} (3\cos\alpha - 2) \right\}^{-1}$$

where the design parameters—E_{PMMA}, t, w, L, and α—are as defined in Fig. 4.1(b). Note that this equation is derived based on a single-material-based cantilever beam, assuming isometric and symmetric sections and its neutral axis located at the geometric centroid, thus producing a uniform mechanical behavior. When Au and Cr are added on PMMA, albeit very thin, the analytical k_{eff} values obtained using above equation would be inaccurate. In order to account for different dimensions and properties of the materials composing the cantilever, numerical simulation software (CoventorWare® 10 [66], which uses the finite element method) is used to estimate k_{eff} values (Fig. 4.7). The analytical and simulated values are consistent with the experimental values within ±10 %. The difference between the predicted and experimental values can be attributed to process-induced variations and approximations in the design parameters and material properties in simulations and calculations.

Chapter 5

CONCLUSIONS

We have proposed and demonstrated polymer-based cantilever probes in order to enable AFM-based biological research requiring non-invasive, high-speed, broad-band nanomechanical measurements of live mammalian cells in liquid. V-shaped and rectangular prototype cantilever probes have been implemented using a surface-micromachining process and bio-compatible materials. The adhesive-based assembly method would allow low-cost rapid prototyping of soft cantilever probes, yet at the expense of device-to-device uniformity. Finite element analysis, analytic equations, and thermal noise analysis have been employed to determine the physical properties of the fabricated prototypes. One of the V-shaped prototypes has been installed into the AFM system to conduct nanoindentation tests on live HeLa cells in liquid. The measurement results obtained with the prototype have been compared against with a Si_3N_4 cantilever probe. It has been observed that negligible deformation/distortion of the cell membrane has occurred when the polymer probe was employed. For further AFM-based biological studies, the design and fabrication process of the prototype probe are fine-tuned. We achieved a sharp tip with a radius of curvature as small as 40 nm, which is comparable to that of a commercial Si-based probe, via sequential depositions of low- and high-viscosity PMMA. We also achieved a relatively flat cantilever with a strain gradient as low as $\sim 10^{-4}$ μm^{-1} by properly confining the optical reflection coating only at tip region. We achieved an effective spring constant of ~0.01 N/m, which is about an order of magnitude smaller than that of a Si-based probe. With further design refinements and fabrication process improvements and with biological experiments that validate the application of the probe, the proposed AFM probe might be a promising choice that enables AFM-based biological research requiring non-invasive high-speed high-resolution topographical imaging and nanomechanical measurements on live cells in a liquid culture medium.

Reference

[1] D. Müller and Y. Dufrene, "Atomic force microscopy as a multifunctional molecular toolbox in nanobiotechnology," *Nature nanotechnology*, vol. 3, no. 5, pp. 261–269, 2008.

[2] J. K. H. Hörber and M. J. Miles, "Scanning probe evolution in biology," *Science*, vol. 302, pp. 1002–1005, 2003.

[3] D. Müller and Y. Dufrene, "Atomic force microscopy: a nanoscopic window on the cell surface," *Trends in cell biology*, vol. 21, no. 8, pp. 461–469, 2011.

[4] T. G. Kuznetsova, M. N. Starodubtseva, N. I. Yegorenkov, S. A. Chizhik, and R. I. Zhdanov, "Atomic force microscopy probing of cell elasticity," *Micron*, vol. 38, no. 8, pp. 824–833, 2007.

[5] K. Tomankova, P. Kolar, J. Malohlava, and H. Kolarova, "Mechanical characterization of HeLa cells using atomic force microscopy," in *Current Microscopy Contributions to Advances in Science and Technology*, A. Méndez-Vilas, Ed. Badajoz: Formatex Research Center, 2012, pp. 549–554.

[6] Q. S. Li, G. Y. H. Lee, C. N. Ong, and C. T. Lim, "AFM indentation study of breast cancer cells," *Biochemical and Biophysical Research Communications*, vol. 374, no. 4, pp. 609–613, 2008.

[7] H. J. Butt, B. Cappella, and M. Kappl, "Force measurements with the atomic force microscope: Technique, interpretation, and applications," *Surface Science Reports*, vol. 59, no. 1, pp. 1–152, 2005.

[8] S. A. S. Asif, K. J. Wahl, R. J. Colton, and O. L. Warren, "Quantitative imaging of nanoscale mechanical properties using hybrid nanoindentation and force modulation," *Journal of Applied Physics*, vol. 90, no. 3, pp. 1192–1200, 2001.

[9] J. Skommer, Z. Darzynkiewicz, and D. Wlodkowic, "Cell death goes LIVE: technological advances in real-time tracking of cell death," *Cell Cycle*, vol. 9, no. 12, pp. 2330–2341, 2010.

[10] J. Z. Rappoport and S. M. Simon, "Real-time analysis of clathrin-mediated endocytosis during cell migration," *Journal of Cell Science*, vol. 116, no. 5, pp. 847–855, 2003.

[11] I. Sokolov, "Atomic force microscopy in cancer cell research," *Cancer Nanotechnology*, vol. 1, pp. 1–17, 2007.

[12] J. D. Adams, B. W. Erickson, J. Grossenbacher, J. Brugger, A. Nievergelt, and G. E. Fantner, *Nature Nanotechnology*, vol. 11, pp. 147–151, 2016.

[13] F. Yu, J. Liu, S. Yu, Z. Yang, Y. Pan, N. Gao, Q. Zou, and J. Jeon, "Soft polymer-based cantilever probe for AFM nanoindentation of live mammalian cells in liquid," in *the 18th International Conference on Solid-State Sensors, Actuators and Microsystems (Transducers)*, pp. 2260-2263, 2015.

[14] J. Alcaraz, L. Buscemi, M. Grabulosa, X. Trepat, B. Fabry, R. Farré, and D. Navajas, "Microrheology of human lung epithelial cells measured by atomic force microscopy," *Biophysical journal*, vol. 84, no. 3, pp. 2071–2079, 2003.

[15] B. A. Smith, B. Tolloczko, J. G. Martin, and P. Grütter, "Probing the viscoelastic behavior of cultured airway smooth muscle cells with atomic force microscopy: stiffening induced by contractile agonist," *Biophysical journal*, vol. 88, no. 4, pp. 2994–3007, 2005.

[16] M. J. Rosenbluth, W. A. Lam, and D. A. Fletcher, "Force microscopy of nonadherent cells: a comparison of leukemia cell deformability," *Biophysical journal*, vol. 90, no. 8, pp. 2994–3003, 2006.

[17] H. Schillers, M. Wälte, K. Urbanova, and H. Oberleithner, "Real-time monitoring of cell elasticity reveals oscillating myosin activity," *Biophysical journal*, vol. 99, no. 11, pp. 3639–3646, 2010.

[18] J. Zou, X. Wang, D. Bullen, K. Ryu, C. Liu, and C. A. Mirkin, "A Mould-and-Transfer Technology for Fabricating Scanning Probe Microscopy Probes," *Journal of Micromechanics and Microengineering*, vol. 14, pp. 204–211, 2004.

[19] B. A. Smith, B. Tolloczko, J. G. Martin, and P. Grütter, "Soft, Entirely Photoplastic Probes for Scanning Force Microscopy," *Review of Scientific Instruments*, vol. 70, no. 5, pp. 2398–2401, 1999.

[20] R. Pechmann, J. M. Köhler, W. Fritzsche, A. Schaper, and T. M. Jovin, "The Novolever: A New Cantilever for Scanning Force Microscopy Microfabricated from Polymeric Materials," *Review of Scientific Instruments*, vol. 65, no. 12, pp. 3702–3706, 1994.

[21] M. Nordström, S. Keller, M. Lillemose, A. Johansson, S. Dohn, D. Haefliger, G. Blagoi, M. Havsteen-Jakobsen, and A. Boisen, "SU-8 Cantilevers for Bio/Chemical Sensing; Fabrication, Characterization and Development of Novel Read-out Methods," *Sensors*, vol. 8, no. 3, pp. 1595–1612, 2008.

[22] M. Tortonese, "Cantilevers and Tips for Atomic Force Microscopy," *IEEE Engineering in Medicine and Biology Magazine*, vol. 16, pp. 28–33, 1997.

[23] R. Q. Frazer, R. T. Byron, P. B. Osborne, and K. P. West, "PMMA: An Essential Material in Medicine

and Dentistry," *Journal of Long-Term Effects of Medical Implants*, vol. 15, no. 6, pp. 629–639, 2005.
[24] G. Voskerician, M. S. Shive, R. S. Shawgo, H. Recum, J. M. Anderson, M. J. Cima, and R. Langer, "Biocompatibility and Biofouling of MEMS Drug Delivery Devices," *Biomaterials*, vol. 24, no. 11, pp. 1959–1967, 2003.
[25] R. T. Moretti-Neto, I. Mello, A. B. S. Moretti, C. R. C. Robazza, and A. A. C. Pereira, "In-Vivo Qualitative Analysis of the Biocompatibility of Different Cyanoacrylate-Based Adhesives," *Brazilian Oral Research*, vol. 22, no. 1, pp. 43–47, 2008.
[26] J. W. Gooch, *Biocompatible Polymeric Materials and Tourniquets for Wounds*. New York, NY, USA: Springer Science and Business Media, 2010, p. 62.
[27] S. Akamine and C. F. Quate, "Low Temperature Thermal Oxidation Sharpening of Microcast Tips," *Journal of Vacuum Science and Technology B*, vol. 10, no. 5, pp. 2307–2310, 1992.
[28] Microchem Corp., "NANO PMMA and Copolymer," PMMA data sheet, 2001.
[29] S. H. Goods, "Thermal Expansion and Hydration Behavior of PMMA Moulding Materials for LIGA Applications," Sandia National Laboratories, Albuquerque, NM, Rep. SAND2003-8000, 2003.
[30] *Coefficients of Linear Thermal Expansion*. [Online]. Available: http://www.engineeringtoolbox.com/linear-expansion-coefficients-d_95.html
[31] G. Dhatt, E. Lefrançois, and G. Touzot, *Finite Element Method*, Hoboken, NJ, USA: John Wiley & Sons, 2012.
[32] N. A. Burnham, X. Chen, C. S. Hodges, G. A. Matei, E. J. Thoreson, C. J. Roberts, M. C. Davies, and S. J. B. Tendler, "Comparison of Calibration Methods for Atomic-Force Microscopy Cantilevers," *Nanotechnology*, vol. 14, no. 1, pp. 1–6, 2003.
[33] J. L. Hutter and J. Bechhoefer, "Calibration of Atomic Force Microscope Tips," *Review of Scientific Instruments*, vol. 64, no. 7, pp. 1868–1873, 1993.
[34] C. V. Heer, *Statistical Mechanics Kinetic Theory, and Stochastic Processes*. New York, NY, USA: Academic Press Inc., 1972, p. 431.
[35] H.-J. Butt, P. Siedle, K. Seifert, K. Fendler, T. Seeger, E. Bamberg, A. L. Weisenhorn, K. Goldie, and A. Engel, *Journal of Microscopy*, vol. 169, no. 75, pp. 75–84, 1993.
[36] J. E. Sader and L. White, "Theoretical analysis of the static deflection of plates for atomic force microscope applications," *Journal of Applied physics*, vol. 74, no. 1, pp. 1–9, 1993.
[37] J. E. Sader, "Parallel beam approximation for V-shaped atomic force microscope cantilevers," *Review of Scientific Instruments*, vol. 66, no. 9, pp.4583–4587, 1995.
[38] T. R. Albrecht, S. Akamine, T. E. Carver, and C. F. Quate, "Microfabrication of cantilever styli for the atomic force microscope," *Journal of Vacuum Science & Technology A*, vol. 8, no. pp. 3386–3396, 1990.
[39] G. M. Rebeiz, *RF MEMS Theory, Design, & Technology*. John Wiley and Sons, Hoboken, NJ, USA, 2003, p. 29.
[40] M. Stafford, B. D. Vogt, C. Harrison, D. Julthongpiput, and R. Huang, "Elastic Moduli of Ultrathin Amorphous Polymer Films," *Macromolecules*, vol. 39, no. 15, pp. 5095–5099, 2006.
[41] *Young's modulus of chromium*. [Online]. Available: https://www.webelements.com/chromium/physics.html
[42] *Young's modulus of gold*. [Online]. Available: https://www.webelements.com/gold/physics.html
[43] R. Kalluri and R.A. Weinberg, "The Basics of Epithelial-Mesenchymal Transition," *The Journal of Clinical Investigation*, vol. 119, no. 6, pp. 1420–1428, 2009.
[44] J. P. Thiery and J. P. Sleeman, "Complex Networks Orchestrate Epithelial-Mesenchymal Transitions," *Nature Reviews Molecular Cell Biology*, vol. 7, no. 2, pp. 131–142, 2006.
[45] J. Ren, S. Yu, N. Gao, and Q. Zou, "Indentation Quantification for In-Liquid Nanomechanical Measurement of Soft Material Using an Atomic Force Microscope: Rate-Dependent Elastic Modulus of Live Cells," *Physical Review E*, vol. 88, no. 5, pp. 052711–052722, 2013.
[46] B. Bhushan, *Nanotribology and Nanomechanics I: Measurement Techniques and Nanomechanics*. New York, NY, USA: in Springer Science and Business Media, 2010, p. 784.
[47] A. Khan, J. Philip, and P. Hess, "Young's Modulus of Silicon Nitride Used in Scanning Force Microscope Cantilevers," *Journal of Applied Physics*, vol. 95, no. 4, pp. 1667–1672, 2004.
[48] P. Walsh, A. Omeltchenko, R. K. Kalia, A. Nakano, P. Vashishta, and S. Saini, "Nanoindentation of Silicon Nitride: A Multimillion-Atom Molecular Dynamics Study," *Applied Physics Letters*, vol. 82, no. 1, pp. 118–120, 2003.
[49] B. Bhushan, *Scanning Probe Microscopy in Nanoscience and Nanotechnology*. Springer Science and

Business Media, NY, USA, 2010, p. 230.
[50] F. Yu, J. Liu, S. Yu, N. Gao, Q. Zou, and J. Jeon, "Polymer-Based Cantilever Probe for Nanomechanical Characterization of Live Mammalian Cells with Atomic Force Microscope," under review of Journal of Microelectromechanical Systems.
[51] L. Zhang, Lecture 10: *Basics of Atomic Force Microscope (AFM)*. [Online]. Available: http://www.eng.utah.edu/~lzang/images/Lecture_10_AFM.pdf
[52] B. Bhushan, *Modern Tribology Handbook*, CRC Press, Boca Raton, FL, USA, 2000, Ch. 17.
[53] C. Lee, X. Wei, J. W. Kysar, and J. Hone, "Measurement of the elastic properties and intrinsic strength of monolayer graphene," *Science*, vol. 321, no. 5887, pp. 385–388, 2008.
[54] *Certificate of Analysis*, 495 PMMA, 950 PMMA, MicroChem Corporation, 2015.
[55] *Reynolds Number*. [Online]. Available: http://www.grc.nasa.gov/WWW/BGH/reynolds.html
[56] G. K. Batchelor, *An Introduction to Fluid Dynamics*. Cambridge University Press, Cambridge, UK, 2000, p. 174.
[57] *Electron beam evaporation*. [Online]. Available: http://www.tungsten.com/tips/electron-beam-evaporation/
[58] A. K. Sinha, H. J. Levinstein, and T. E. Smith, "Thermal stresses and cracking resistance of dielectric films (SiN, Si3N4, and SiO2) on Si substrates," J*ournal of applied physics*, vol. 49, no. 4, pp. 2423–2426, 1978.
[59] *Coefficient of thermal expansion of silicon dioxide*. [Online]. Available: http://www.azom.com/properties.aspx?ArticleID=1114
[60] *Coefficients of Linear Thermal Expansion of chromium and gold*. [Online]. Available: http://www.engineeringtoolbox.com/linear-expansion-coefficients-d_95.html
[61] *Poisson ration of chromium and gold*. [Online]. Available: http://periodictable.com/Properties/A/PoissonRatio.v.html
[62] P. Chen, P. Raghavan, K. Yazzie, and H. Fei, "On the effective coefficient of thermal expansion (CTE) of bilayer/trilayer in semiconductor package substrates," in *IEEE 65th Electronic Components and Technology Conference (ECTC)*, pp. 1932–1937, 2015.
[63] M. Gad-el-Hak, *The MEMS Handbook*. CRC Press, Boca Raton, FL, USA, 2000, Ch. 16, p. 127.
[64] V. L. Spiering, S. Bouwstra, R. M. E. J. Spiering, and M. Elwenspoek, in *1991 International Conference on Solid-State Sensors and Actuators (Transducers)*, 982–985, 1991.
[65] S. D. Senturia, *Microsystem Design*. Kluwer Academic Publishers, 2001, pp. 201–238.
[66] CoventorWare Reference Manual, Coventor, Cary, NC, USA, 2008.